Magnetic order in the rare-earth ferroborate $CeFe_3(BO_3)_4$

Shohei Hayashida,[1] Shinichiro Asai,[1] Daiki Kato,[1] Shunsuke Hasegawa,[1] Maxim Avdeev,[2,3] Huibo Cao,[4] and Takatsugu Masuda[1]

[1]*Institute for Solid State Physics, The University of Tokyo, Chiba 277-8581, Japan*
[2]*Australian Nuclear Science and Technology Organisation, Menai, NSW 2234, Australia*
[3]*School of Chemistry, The University of Sydney, Sydney, NSW 2006, Australia*
[4]*Neutron Scattering Division, Oak Ridge National Laboratory, Oak Ridge, Tennessee 37831, USA*

(Received 15 June 2018; revised manuscript received 7 October 2018; published 4 December 2018)

We have studied the magnetic order of the rare-earth ferroborate $CeFe_3(BO_3)_4$ through the thermodynamic and the neutron diffraction measurements. The heat capacity and the magnetic susceptibility revealed antiferromagnetic magnetic ordering at 29 K. In the neutron powder diffraction data, we observed the magnetic Bragg peaks indexed by the commensurate (CM) propagation vector $\boldsymbol{k}_{\mathrm{CM}} = (0, 0, \frac{3}{2})$ and the incommensurate (ICM) vector $\boldsymbol{k}_{\mathrm{ICM}} = (0, 0, \frac{3}{2} + \delta)$. The incommensurability δ increases with decreasing the temperature, and is evaluated to be 0.04556(16) at 3.7 K. Magnetic structure analysis reveals that the magnetic moments aligning in the ab plane form the collinear antiferromagnetic structure having $\boldsymbol{k}_{\mathrm{CM}}$ and helical structure having $\boldsymbol{k}_{\mathrm{ICM}}$. Detailed measurements of the magnetic susceptibility exhibit an additional anomaly at 27 K. Furthermore, the temperature dependence of the neutron diffraction profile on the single-crystal sample shows that the ICM and CM ordering occurs at 29 and 26 K, respectively. These results suggest a phase separation state between the collinear and helical structures. The multiferroicity of $CeFe_3(BO_3)_4$ is discussed on the basis of the determined magnetic structure.

DOI: 10.1103/PhysRevB.98.224405

I. INTRODUCTION

Multiferroicity has been a central topic in condensed matter physics due to nontrivial magnetoelectric (ME) effects and cross-correlation phenomena which can be utilized in future electronics. Since the discovery of the multiferroicity in the perovskite $TbMnO_3$ [1], various compounds have been found, reviews of which can be found in Refs. [2–4]. The microscopic origin of the spin-driven multiferroicity has been established by both theoretical and experimental studies [5–9]. Because the magnetic structure plays an important role in the induction of the electric polarization, the identification of the magnetic structure is crucial for understanding multiferroics [10].

The family of rare-earth ferroborates $RFe_3(BO_3)_4$ (R = rare-earth metal or Y) is a new series of the multiferroic compounds containing R^{3+} ($4f^n$) and Fe^{3+} ($3d^5$ $S = 5/2$) as magnetic ions. The variety of the magnetic anisotropies of the R^{3+} ion and the interaction between the Fe^{3+} and R^{3+} moments (f-d coupling) lead to diverse ME effects [11–19], the mechanism of which is explained by the spin-dependent metal-ligand hybridization model [20,21]. Many types of the magnetic structures have been identified depending on the species of the R^{3+} ions [22–30]. They are roughly classified into the easy-axis and easy-plane type structures. The compounds having the former type show large electric polarization: ~300 $\mu C/m^2$ for $NdFe_3(BO_3)_4$ [12] and ~400 $\mu C/m^2$ for $SmFe_3(BO_3)_4$ [18]. Furthermore, intriguing characters including quadrupole helix chirality [31], nontrivial manifestation of electron-phonon coupling [32], and electric- and magnetic-field control of magnons [33] have been found in recent studies. The rare-earth ferroborates are thus fascinated series of the multiferroic compounds.

The crystal structure of the rare-earth ferroborates is trigonal with the space group $R32$ as shown in Fig. 1, which belongs to the structural type of mineral huntite $CaMg_3(CO_3)_4$ [34]. The main feature is that the FeO_6 octahedra form spiral chains with threefold symmetry along the crystallographic c axis. Among the rare-earth ferroborates, $CeFe_3(BO_3)_4$ has been less focused on; a brief report on a magnetic long-range order on the polycrystalline sample by means of the heat capacity and magnetic susceptibility measurements, to our knowledge, is the only publication [35].

In the present paper the thermodynamic properties and magnetic structure of $CeFe_3(BO_3)_4$ are studied. Following the Introduction, we describe the experimental details on the sample preparation and the experimental setups of the thermodynamic and neutron diffraction measurements in Sec. II. The heat capacity and magnetic susceptibility of the single-crystal sample $CeFe_3(BO_3)_4$ are shown in Sec. III. The neutron diffraction profiles of the polycrystalline and single-crystal samples of $CeFe_3(^{11}BO_3)_4$ are demonstrated in Sec. IV. The magnetic structure is determined using representation analysis and Rietveld refinement in Sec. V. The multiferroicity of $CeFe_3(BO_3)_4$ is discussed in Sec. VI. The conclusions are given in Sec. VII.

II. EXPERIMENTAL DETAILS

The single-crystal sample was grown by a flux method [36]. In advance we synthesized polycrystalline samples from

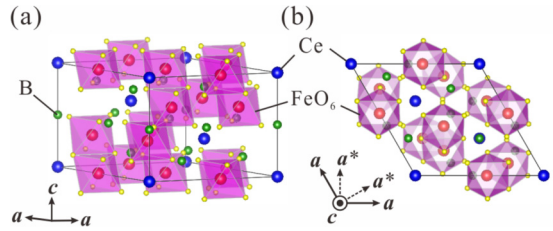

FIG. 1. The crystal structures of $CeFe_3(BO_3)_4$ (trigonal, space-group $R32$). FeO_6 octahedra form the spiral chains along the c axis, and Ce^{3+} ions are located between the chains.

the starting materials: CeO_2, Fe_2O_3, and B_2O_3. The stoichiometric amounts of the starting materials were mixed, ground, and put into an alumina crucible. The crucible was heated at 1000 °C for 72 h in total to obtain the polycrystalline sample. The flux is $Bi_2Mo_3O_{12}$ + 3 B_2O_3 + 6/5 CeO_2. $Bi_2Mo_3O_{12}$ was synthesized by the solid state reaction from Bi_2O_3 and MoO_3 in an alumina crucible at 600 °C for 24 h. A mixture of the polycrystalline $CeFe_3(BO_3)_4$ and the flux with the mass ratio of 1:4 was put into a platinum crucible inside the alumina crucible. The crucibles were heated to 1000 °C for 4 h, kept at this temperature for 6 h, cooled to 962 °C for 1 h, and slowly cooled down to 870 °C for 120 h. Then the furnace was shut down, and naturally cooled down to room temperature. The flux was removed by HCl solution.

The heat capacity was measured with a Physical Properties Measurement System (PPMS, Quantum Design) in the temperature range from 1.8 to 320 K. Magnetic characterization was performed using a commercial SQUID magnetometer (MPMS, Quantum Design) for temperatures between 1.8 and 300 K.

For the neutron diffraction experiment, a polycrystalline sample of $CeFe_3(^{11}BO_3)_4$, in which 99% of the natural B was enriched by the ^{11}B, was prepared by pulverizing small single crystals to obtain a high quality sample. The total mass of the sample was 2.9 g. We put the polycrystalline sample in a vanadium cell and the cell was installed in the closed cycle refrigerator. We used the high resolution powder diffractometer ECHIDNA installed at the OPAL research reactor operated by the Australian Nuclear Science and Technology Organisation (ANSTO). We chose a Ge-331 monochromator to obtain the neutrons with the wavelength of 2.4395 Å, and used the open-open-5' configuration. The neutron powder diffraction data were collected in the temperature range from 3.6 to 50 K. The obtained profiles were analyzed by the Rietveld method using the FULLPROF software [37]. Candidates for the magnetic structure compatible with the lattice symmetry were obtained by the SARAh software [38].

Single-crystal neutron diffraction was performed on the HB-3A Four-Circle Diffractometer equipped with a two-dimensional detector at the High Flux Isotope Reactor (HFIR) at the Oak Ridge National Laboratory (ORNL). Neutron wavelength of 1.546 Å was used from a bent perfect Si-220 monochromator [39]. The mass of the single-crystal of $CeFe_3(^{11}BO_3)_4$ was 23 mg. The sample was installed in a closed cycle refrigerator. The measured temperature range was 5–30 K.

III. THERMODYNAMIC PROPERTIES

The temperature dependence of the heat capacity on the single-crystal sample is shown in Fig. 2(a). A λ-type anomaly is observed at 29 K indicating magnetic long-range ordering. This is consistent with the heat capacity measurement on the polycrystalline sample in the previous study [35]. In contrast to other rare-earth ferroborates including Eu-, Gd-, Tb-, and Dy-ferroborates which exhibit structural phase transition below 300 K [35,40–42], no structural transition is found down to 1.8 K.

The phonon contribution has been estimated by fitting the high-temperature data above 90 K. The phonon contribution C_{phonon} is provided by

$$C_{\text{phonon}}\ (\text{J mol}^{-1}) = AC_{\text{D}} + (n - A)C_{\text{E}}, \tag{1}$$

where C_{D} and C_{E} are Debye- and Einstein-type heat capacities, respectively. n is the number of the atoms in the formula unit, 20, and A is the ratio of C_{D} to C_{E}. The calculated curve gives reasonable agreement with the experimental data as shown in Fig. 2(a). The parameters are obtained as the $A = 11.0$, $T_{\text{D}} = 451$ K, and $T_{\text{E}} = 1139$ K, where the T_{D} and T_{E} are Debye and Einstein temperatures, respectively. The magnetic heat capacity divided by the temperature C_{m}/T is thus obtained by subtracting the phonon contribution as shown in Fig. 2(b). A Schottky-like anomaly is found at about 10 K, which is due to the split of the Kramers doublet of the ground state of the Ce^{3+} ion by the molecular field from the ordered Fe^{3+} subsystem. This means that the Ce^{3+} moment interacts with the Fe^{3+} moment as reported in other rare-earth ferroborates [41–47]. The magnetic entropy is evaluated by

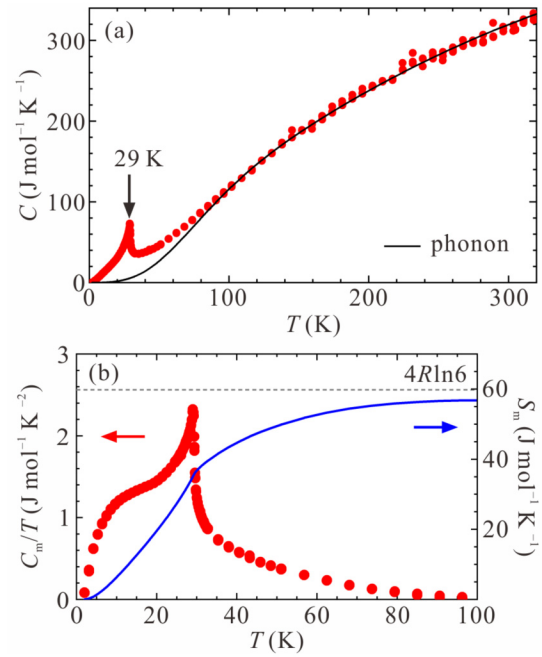

FIG. 2. (a) Temperature dependence of heat capacity at zero magnetic field. The solid curve represents the phonon contribution estimated from fitting the data at $T > 90$ K. (b) Temperature dependence of magnetic heat capacity C_{m}/T (red marks; left axis) and entropy S_{m} (blue curve; right axis).

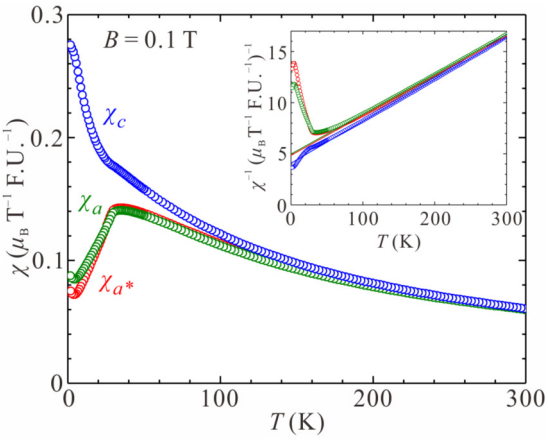

FIG. 3. Temperature dependence of the magnetic susceptibilities along the a, a^*, and c axes at $B = 0.1$ T. Inset shows the inverse susceptibilities χ^{-1}. The solid line on the χ^{-1} represents Curie-Weiss fits to the data in the range of $80 < T < 300$ K, which gives Weiss temperatures of $-124.5(4)$ K for χ_a, $-127.5(3)$ K for χ_{a^*}, and $-99.2(3)$ K for χ_c. The effective magnetic moments are $10.71(1)\ \mu_B$ for χ_a, $10.70(1)\ \mu_B$ for χ_{a^*}, and $10.42(1)\ \mu_B$ for χ_c.

$S_m(T) = \int_0^T C_m(T)/T\ dT$ as indicated by the blue curve in Fig. 2(b). The total magnetic entropy for the total angular momentum $J = 5/2$ of the Ce^{3+} ion and spin $S = 5/2$ of the Fe^{3+} ion in 1 mol of $CeFe_3(BO_3)_4$ is expected to be $4R \ln 6 = 59.6\ J\ mol^{-1}\ K^{-1}$, where R is the gas constant. We notice that $S_m(100\ K)$ reaches 95% of the total entropy. The magnetic entropy at $T_N = 29$ K is $35.0\ J\ mol^{-1}\ K^{-1}$, which is comparable to $R(\ln 2 + 3 \ln 6) = 50.5\ J\ mol^{-1}\ K^{-1}$ on the basis of one Kramers doublet of the Ce^{3+} ion and three spins of $S = 5/2$ of the Fe^{3+} ions. Thus, the Kramers doublet of the Ce^{3+} ion and spin $S = 5/2$ of the Fe^{3+} ion are responsible for the magnetic dynamics in the low energy at low temperatures. $S_m(T_N)$ is less than $R(\ln 2 + 3 \ln 6)$ is likely due to the entropy being released by the development of short-range magnetic correlation above T_N.

The temperature dependence of the magnetic susceptibilities along the a, a^*, and c axes, χ_a, χ_{a^*}, and χ_c, is shown in Fig. 3. Above 80 K, the susceptibilities follow the Curie-Weiss law. A deviation from the Curie-Weiss law observed in the range of $30 < T < 80$ K is due to the development of the short-range magnetic correlation on approaching the T_N. The Curie-Weiss fit in the range of $80 \leqslant T \leqslant 300$ K yields the Weiss temperatures of $-124.5(4)$ K for χ_a, $-127.5(3)$ K for χ_{a^*}, and $-99.2(3)$ K for χ_c. The effective magnetic moments are $10.71(1)\ \mu_B$ for χ_a, $10.70(1)\ \mu_B$ for χ_{a^*}, and $10.42(1)\ \mu_B$ for χ_c. The theoretical value of the effective magnetic moment is calculated from the equation

$$\mu_{calc}^2 = \mu_{eff}(Ce^{3+})^2 + 3\mu_{eff}(Fe^{3+})^2. \quad (2)$$

The effective moments $\mu_{eff}(Ce^{3+})$ having $J = 5/2$ and $\mu_{eff}(Fe^{3+})$ having $S = 5/2$ are given by

$$\mu_{eff}(Ce^{3+}) = g_J\sqrt{J(J+1)} = 2.54\ \mu_B, \quad (3)$$

$$\mu_{eff}(Fe^{3+}) = 2\sqrt{S(S+1)} = 5.92\ \mu_B. \quad (4)$$

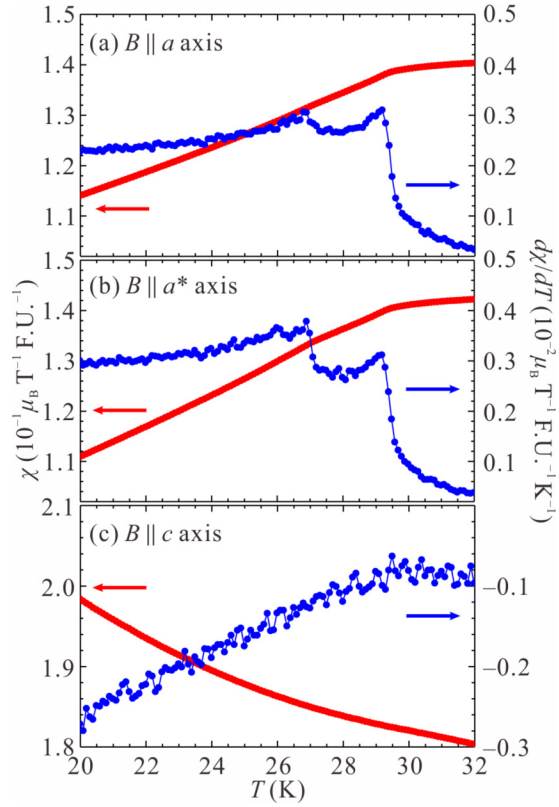

FIG. 4. Magnetic susceptibilities and their derivatives along the a, a^*, and c axes in (a), (b), and (c), respectively. The applied magnetic fields are 0.1 T.

Here g_J is the Landé g factor, which is 6/7 for the Ce^{3+} ion having $S = 1/2$, $L = 3$, and $J = 5/2$. The theoretical effective moment is thus $\mu_{calc} = 10.6\ \mu_B$, which agrees with the obtained effective moments from the experiment. It is found that the out-of-plane susceptibility χ_c is larger than the in-plane susceptibility χ_a or χ_{a^*} in the paramagnetic phase, which can be ascribed to an anisotropic g tensor of the Ce^{3+} moments. The anisotropy ratio χ_c/χ_{ab} increases with decreasing the temperature.

The noticeable change is found in the $\chi(T)$ at about 30 K due to onset of the magnetic long-range order. The decrease of χ_a and χ_{a^*} with the temperature below T_N suggests that the magnetic structure of $CeFe_3(BO_3)_4$ is antiferromagnetic with the magnetic moments oriented in the ab plane. Whereas $NdFe_3(BO_3)_4$ has the easy axis along the a axis [24], the small difference between χ_a and χ_{a^*} of $CeFe_3(BO_3)_4$ does not allow a final conclusion from the magnetization data as to the orientation of the easy axis in the ab plane. $\chi_c(T)$ exhibits an upturn behavior below T_N. This may be due to a small canting and a small moment component along the c axis.

The detailed structures of the susceptibilities and their derivatives in the range of $20 \leqslant T \leqslant 32$ K are shown in Fig. 4. As expected, anomalies in $d\chi_a/dT$, $d\chi_{a^*}/dT$, and $d\chi_c/dT$ are observed at 29 K, which corresponds to the antiferromagnetic transition temperature T_N. Additional peak anomalies are found at 27 K in $d\chi_a/dT$ and $d\chi_{a^*}/dT$, even though no anomaly is observed in the heat capacity. This

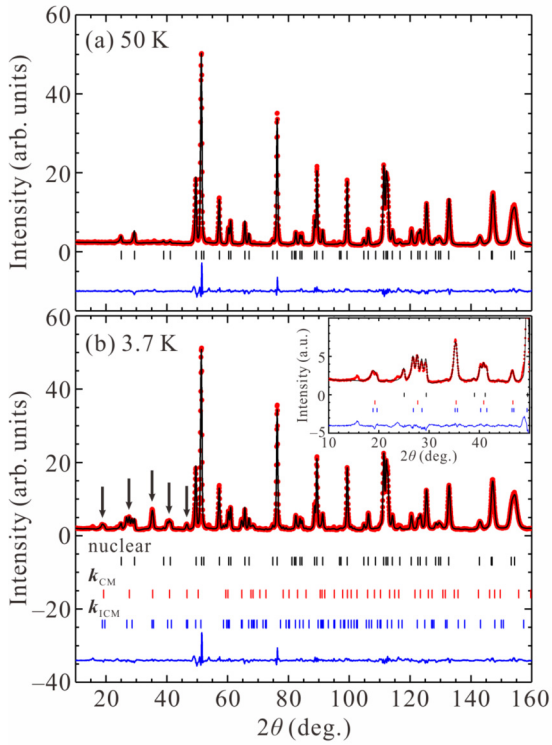

FIG. 5. Neutron diffraction profiles for $CeFe_3(^{11}BO_3)_4$ at 50 K (a) and 3.7 K (b). The inset shows the profile at 3.7 K expanded in the range of $10^\circ \leqslant 2\theta \leqslant 50^\circ$. The solid squares and curves show the experimental data and simulations, respectively. The vertical bars show the position of the nuclear and magnetic Bragg peaks. The solid curves below the bars show the difference between the data and simulations. The arrows indicate the magnetic Bragg peaks.

implies that the magnetic structure changes in the ab plane without a substantial release of the magnetic entropy.

IV. NEUTRON DIFFRACTION

Figure 5(a) shows the neutron diffraction profile measured at 50 K. This profile is reasonably fitted by the hexagonal structure with the space group $R32$. The profile factors are $R_{wp} = 6.36\%$ and $R_{exp} = 1.84\%$. The lattice parameters are $a = 9.60232(6)$ and $c = 7.63129(5)$ Å and the obtained structural parameters are listed in Table I.

At 3.7 K, additional peaks are observed as shown in Fig. 5(b). The peak intensities increase with decreasing the temperature below 30 K as shown in Fig. 6. This confirms

TABLE I. Structural parameters of $CeFe_3(^{11}BO_3)_4$ at $T = 50$ K.

Atom	Site	x	y	z
Ce	3*a*	0	0	0
Fe	9*d*	0.5525(3)	0	0
O	9*e*	0.8566(3)	0	1/2
O	9*e*	0.5892(3)	0	1/2
O	18*f*	0.4499(2)	0.1428(3)	0.5193(2)
B	3*b*	0	0	1/2
B	9*e*	0.4473(3)	0	1/2

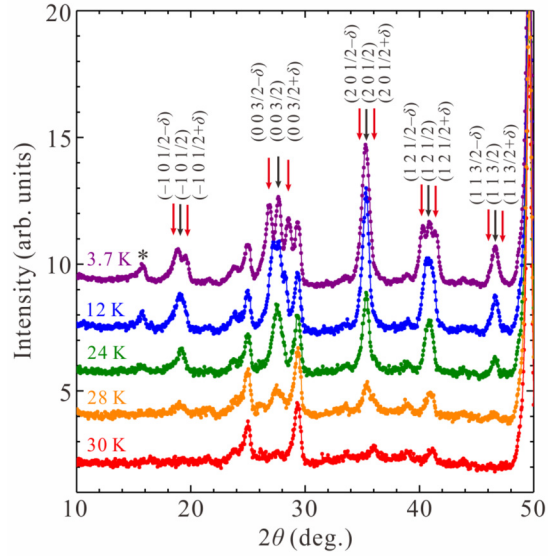

FIG. 6. Temperature evolution of the neutron diffraction profiles for $CeFe_3(^{11}BO_3)_4$. The black and red arrows indicate the CM and ICM Bragg peaks. Incommensurability at 3.7 K is $\delta = 0.04556(16)$. The asterisk indicates an unidentified peak.

that the magnetic long-range order develops below T_N. The peaks at $2\theta = 19^\circ$, 28°, 35°, 41°, and 47° are indexed as $(-1\,0\,\frac{1}{2})$, $(0\,0\,\frac{3}{2})$, $(2\,0\,\frac{1}{2})$, $(1\,2\,\frac{1}{2})$, and $(1\,1\,\frac{3}{2})$, and their satellites with $(0\,0\,\pm\delta)$. δ is an incommensurability which is evaluated to be $\delta = 0.04556(16)$ at 3.7 K. The magnetic propagation vectors are thus obtained as a CM vector $\boldsymbol{k}_{CM} = (0, 0, \frac{3}{2})$ and an ICM vector $\boldsymbol{k}_{ICM} = (0, 0, \frac{3}{2} + \delta)$. It is noted that the peak at $2\theta \sim 16^\circ$ in Fig. 6 is not indexed by these propagation vectors. We have surveyed the database of impurities, but this peak cannot be identified.

Figure 7(a) shows the temperature evolution of the neutron diffraction profiles for the single-crystal $CeFe_3(^{11}BO_3)_4$ at $\boldsymbol{q} = (0, -2, l)$. Three peaks are observed at 5 K, which corresponds to the reflections $(2\,0\,\frac{1}{2})$ and $(2\,0\,\frac{1}{2} \pm \delta)$ in the powder diffraction profile. Fitting the data at 5 K with three Gaussian functions yielded the incommensurability $\delta = 0.0432(5)$, which is consistent with the value $\delta = 0.04556(16)$ obtained at 3.7 K in the powder diffraction experiment. The intensity of the CM peak in the single-crystal diffraction data is weaker than that of the ICM peak, in contrast to the data for the polycrystalline sample, in which CM and ICM peaks had similar intensity (Fig. 6).

The temperature variation of the neutron profiles at $\boldsymbol{q} = (0, -2, l)$ is shown in Fig. 7(b). The incommensurability δ decreases with increasing the temperature, and δ at 27 K is 0.0153(2) as obtained by double Gaussian functions fitting, Fig. 7(a). In addition, the CM peak appears at about 26 K, whereas the ICM peak appears at about 29 K, Fig. 7(b). These temperatures are consistent with those of the peak anomalies in the magnetic susceptibilities in Figs. 4(a) and 4(b).

V. ANALYSIS OF MAGNETIC STRUCTURE

The magnetic structure analysis was performed on the neutron powder diffraction data collected at 3.7 K. The

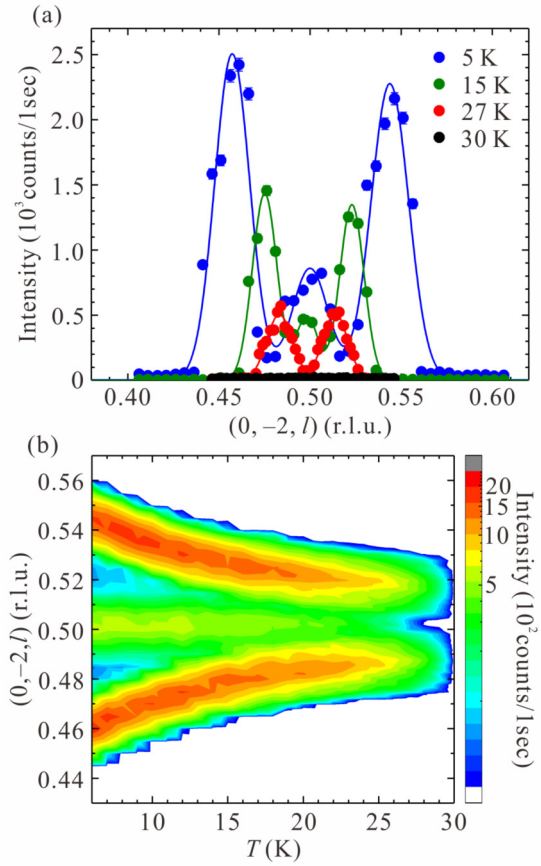

FIG. 7. (a) Temperature evolution of neutron diffraction profiles for the single-crystal $CeFe_3(^{11}BO_3)_4$ at $\boldsymbol{q} = (0, -2, l)$. The solid curves are Gaussian functions. (b) Temperature dependence of the neutron diffraction profiles at $\boldsymbol{q} = (0, -2, l)$.

representation analysis [38] with the space group $R32$ and the propagation vector $\boldsymbol{k}_{\rm CM}$ leads to two irreducible representations (IRs) $\Gamma_2^{\rm Ce} + \Gamma_3^{\rm Ce}$ for the Ce^{3+} ion and three IRs $\Gamma_1^{\rm Fe} + \Gamma_2^{\rm Fe} + 2\Gamma_3^{\rm Fe}$ for the Fe^{3+} ion. The IRs and the basis vectors are summarized in Table II for the Ce^{3+} ion and Table III for the Fe^{3+} ion. The basis vectors for $\Gamma_2^{\rm Ce}$ or $\Gamma_3^{\rm Ce}$ dictate that the Ce^{3+} moment orients along the c axis or in the ab plane, respectively. During testing the models of the magnetic structures were defined by the various IRs, and it was assumed that the magnetic structure is described by a single IR. Under this assumption, we obtain the models for the Fe^{3+} moments as illustrated in Fig. 8. Since the magnetic susceptibility measurements suggested that the magnetic moments lie in the ab plane, we tested six basis vectors corresponding to an easy-plane type structure; $\Psi_1^{\rm Fe}$, $\Psi_2^{\rm Fe}$, $-\Psi_4^{\rm Fe} + \Psi_5^{\rm Fe}$, $-\Psi_7^{\rm Fe} + \Psi_8^{\rm Fe}$, $2\Psi_4^{\rm Fe} + \Psi_5^{\rm Fe}$, and $2\Psi_7^{\rm Fe} + \Psi_8^{\rm Fe}$. In addition, we assume that the ICM structure in the ab plane is the same as that in the CM structure. Since the magnitude of the Ce^{3+} moment is small, we tentatively assume that the direction of the Ce^{3+} moment is parallel to the Fe^{3+} moment in the ab plane.

TABLE II. Basis vectors for the space group $R32$ with $\boldsymbol{k} = (0, 0, \frac{3}{2})$. The atom of the nonprimitive basis are defined according to Ce (0,0,0).

IRs		Basis vectors $[m_a\, m_b\, m_c]$
$\Gamma_2^{\rm Ce}$	$\Psi_1^{\rm Ce}$	[0 0 6]
$\Gamma_3^{\rm Ce}$	$\Psi_2^{\rm Ce}$	$[0\ -\frac{3}{2}\ 0]$
	$\Psi_3^{\rm Ce}$	$[-\sqrt{3}\ -\frac{\sqrt{3}}{2}\ 0]$

TABLE III. Basis vectors for the space group $R32$ with $\boldsymbol{k} = (0, 0, \frac{3}{2})$. The atoms of the nonprimitive basis are defined according to Fe1 (0.5525,0,0), Fe2 (0,0.5525,0), and Fe3 (0.4475,0.4475,0).

IRs		Basis vectors $[m_a\, m_b\, m_c]$		
		Fe1	Fe2	Fe3
$\Gamma_1^{\rm Fe}$	$\Psi_1^{\rm Fe}$	[2 0 0]	[0 2 0]	[−2 −2 0]
$\Gamma_2^{\rm Fe}$	$\Psi_2^{\rm Fe}$	[1 2 0]	[−2 −1 0]	[1 −1 0]
	$\Psi_3^{\rm Fe}$	[0 0 2]	[0 0 2]	[0 0 2]
$\Gamma_3^{\rm Fe}$	$\Psi_4^{\rm Fe}$	$[\frac{1}{2}\ 0\ 0]$	[0 −1 0]	$[-\frac{1}{2}\ \frac{1}{2}\ 0]$
	$\Psi_5^{\rm Fe}$	$[\frac{1}{2}\ \frac{3}{2}\ 0]$	$[0\ \frac{1}{2}\ 0]$	$[-\frac{1}{2}\ 1\ 0]$
	$\Psi_6^{\rm Fe}$	$[0\ 0\ \frac{3}{2}]$	[0 0 0]	$[0\ 0\ -\frac{3}{2}]$
	$\Psi_7^{\rm Fe}$	$[-\frac{\sqrt{3}}{2}\ 0\ 0]$	[0 0 0]	$[-\frac{\sqrt{3}}{2}\ -\frac{\sqrt{3}}{2}\ 0]$
	$\Psi_8^{\rm Fe}$	$[\frac{\sqrt{3}}{2}\ \frac{\sqrt{3}}{2}\ 0]$	$[\sqrt{3}\ \frac{\sqrt{3}}{2}\ 0]$	$[\frac{\sqrt{3}}{2}\ 0\ 0]$
	$\Psi_9^{\rm Fe}$	$[0\ 0\ \frac{\sqrt{3}}{2}]$	$[0\ 0\ -\sqrt{3}]$	$[0\ 0\ \frac{\sqrt{3}}{2}]$

Then the Rietveld refinement of the magnetic structure analysis was performed. First, we tested the multiple-$\boldsymbol{k}$ state having the CM and ICM propagation vectors. The neutron intensity including nuclear and magnetic scatterings $I(\boldsymbol{q})$ is expressed by

$$I(\boldsymbol{q}) = C\left[I_{\rm nuc}(\boldsymbol{q}) + I_{\rm mag}^{\rm CM}(\boldsymbol{q}) + I_{\rm mag}^{\rm ICM}(\boldsymbol{q})\right], \qquad (5)$$

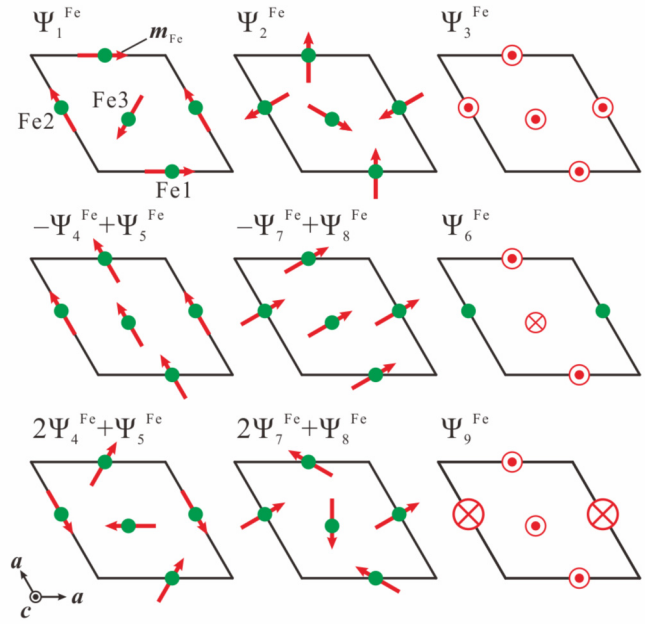

FIG. 8. Schematic representation of the basis vectors $\Psi_i^{\rm Fe}$ with $\boldsymbol{k}_{\rm CM}$ for the Fe^{3+} moments. Magnetic moments are represented by red arrows when they are confined in the ab plane, and by circles when they are along the c axis. In Ψ_9 one large downward moment and two small upward moments in the unit cell cancel the total moment.

where $I_{\rm nuc}(\boldsymbol{q})$ is intensity for the nuclear reflections, and $I_{\rm mag}^{\rm CM}(\boldsymbol{q})$ and $I_{\rm mag}^{\rm ICM}(\boldsymbol{q})$ correspond to the magnetic reflections with $\boldsymbol{k}_{\rm CM}$ and $\boldsymbol{k}_{\rm ICM}$. C is a scale factor. It is found from the Rietveld refinement that only collinear structure in the ab plane with $\boldsymbol{k}_{\rm CM}$ for $\Psi_2^{\rm Ce}$ and $\Psi_3^{\rm Ce}$ in $\Gamma_3^{\rm Ce}$ and for $-\Psi_4^{\rm Fe}+\Psi_5^{\rm Fe}$ and $-\Psi_7^{\rm Fe}+\Psi_8^{\rm Fe}$ in $\Gamma_3^{\rm Fe}$, and helical structure with $\boldsymbol{k}_{\rm ICM}$, where the spin structure in the ab plane is the same as that in the collinear structure, give a satisfactory agreement with the observed profile. The direction of the moments in the ab plane cannot be determined in the collinear structure because of the powder-averaged data. The refined magnitude of the magnetic moments of the Ce^{3+} and Fe^{3+} ions at 3.7 K are $m_{\rm Ce}=0.34(6)\ \mu_{\rm B}$ and $m_{\rm Fe}=2.47(3)\ \mu_{\rm B}$ for $\boldsymbol{k}_{\rm CM}$, and $m_{\rm Ce}=0.02(10)\ \mu_{\rm B}$ and $m_{\rm Fe}=3.34(2)\ \mu_{\rm B}$ for $\boldsymbol{k}_{\rm ICM}$. The moment sizes in this multiple-$\boldsymbol{k}$ structure are not uniform because the direction of the moment for the ICM structure is not orthogonal to that for the CM structure. It should be noted that finite intensity observed at $(0,0,\frac{3}{2})$ means that the CM component is not along the c direction, and that a conical structure having ICM component in the ab plane and CM component in the c direction is not consistent with the experiment.

As shown in Figs. 4(a), 4(b), and 7(b), the onset temperatures of the CM and ICM structures are different, which suggests phase separation. Therefore we analyzed the observed profile by the following phase-separation model. The neutron intensity is represented by

$$I(\boldsymbol{q}) = C\,I_{\rm nuc}(\boldsymbol{q}) + C_1 I_{\rm mag}^{\rm CM}(\boldsymbol{q}) + C_2 I_{\rm mag}^{\rm ICM}(\boldsymbol{q}), \qquad (6)$$

where C_1 and C_2 are scale factors for the CM and ICM domains, and they satisfy that $C=C_1+C_2$. C_1/C_2 corresponds to the ratio of the CM and ICM domains. The scale factor C is independently determined by the nuclear reflections. $I_{\rm mag}^{\rm CM}(\boldsymbol{q})$ and $I_{\rm mag}^{\rm ICM}(\boldsymbol{q})$ are functions of the magnitude of the moments $m_{\rm Ce}$ and $m_{\rm Fe}$, and we assume that the $m_{\rm Ce}$ in the CM and ICM domains are the same and so are the $m_{\rm Fe}$. Then Eq. (6) is represented by

$$I(\boldsymbol{q}) = C\,I_{\rm nuc}(\boldsymbol{q}) + C_1 I_{\rm mag}^{\rm CM}(\boldsymbol{q}; m_{\rm Ce}, m_{\rm Fe}) + (C-C_1) I_{\rm mag}^{\rm ICM}(\boldsymbol{q}; m_{\rm Ce}, m_{\rm Fe}). \qquad (7)$$

Under the additional assumptions described above, we refined C_1, $m_{\rm Ce}$, and $m_{\rm Fe}$. The profiles at 3.7 K and the fitting results are shown in Fig. 5(b). The R factors for the whole profile are $R_{\rm wp}=6.63\%$ and $R_{\rm exp}=1.86\%$. The magnetic R factors $R_{\rm mag}$ for $\boldsymbol{k}_{\rm CM}$ and $\boldsymbol{k}_{\rm ICM}$ are 6.29% and 6.81%. The domain ratio and magnitude of the Ce^{3+} and Fe^{3+} moments are evaluated to be $C_1/C_2=0.567(5)$, $m_{\rm Ce}=0.22(3)\ \mu_{\rm B}$, and $m_{\rm Fe}=4.17(11)\ \mu_{\rm B}$ at 3.7 K. For reference, the best $R_{\rm mag}$ factors in the other basis vectors are listed in Table IV.

So far we have assumed that the magnitude of the Ce^{3+} moment is nonzero and the direction of the Ce^{3+} moment is parallel to the Fe^{3+} moment in the ab plane. Here we test the assumption and check the sensitivity of the refinement for the following models; the Ce^{3+} moment is zero, and the Fe^{3+} and Ce^{3+} moments are canted in the ab plane. In order to avoid the divergence of the parameters, we perform the refinements with the fixed canting angle $\theta_{\text{Ce-Fe}}$ of 30°, 60°, and 90°. The refined magnitude of the Ce^{3+} moment and best $R_{\rm mag}$ factors are listed in Table V. The canted models with $\theta_{\text{Ce-Fe}}=30°$ and 60° are reasonable as well as $\theta_{\text{Ce-Fe}}=0°$. The angle between the Fe^{3+} and Ce^{3+} moments thus cannot be determined.

TABLE IV. The magnetic R factors $R_{\rm mag}$ for $\boldsymbol{k}_{\rm CM}$ and $\boldsymbol{k}_{\rm ICM}$ in each basis vector. The $R_{\rm mag}$ for $-\Psi_4^{\rm Fe}+\Psi_5^{\rm Fe}$ cannot be distinguished from one for $-\Psi_7^{\rm Fe}+\Psi_8^{\rm Fe}$ because of the powder-averaged data.

Basis vector	$R_{\rm mag}(\boldsymbol{k}_{\rm CM})$ (%)	$R_{\rm mag}(\boldsymbol{k}_{\rm ICM})$ (%)
$-\Psi_4^{\rm Fe}+\Psi_5^{\rm Fe}$ $(-\Psi_7^{\rm Fe}+\Psi_8^{\rm Fe})$	6.29	6.81
$\Psi_1^{\rm Fe}$	64.6	63.6
$\Psi_2^{\rm Fe}$	63.9	62.0
$2\Psi_4^{\rm Fe}+\Psi_5^{\rm Fe}$	61.8	59.5
$2\Psi_7^{\rm Fe}+\Psi_8^{\rm Fe}$	51.5	51.7

In the refined magnetic structure with $\boldsymbol{k}_{\rm CM}$, the magnetic moments of the Ce^{3+} and Fe^{3+} ions antiferromagnetically propagate along the c axis in Fig. 9(a), and they ferromagnetically align in the ab plane in Fig. 9(b). The angle between the Fe^{3+} and Ce^{3+} moments in the ab plane is arbitrary. The magnetic structure with $\boldsymbol{k}_{\rm ICM}$ exhibits the helical structure propagating along the c axis as shown in Figs. 9(c) and 9(d). The Fe^{3+} moment of $4.17(11)\ \mu_{\rm B}$ is consistent with $4.2\ \mu_{\rm B}$ in Nd- and Sm-ferroborates [24,25], but it is 84% of the full moment of the Fe^{3+} ion. This may be associated with an existence of the magnetic frustration. The domain ratio C_1/C_2 of 0.567(5) means that the occupation for the helical phase is nearly double of that for the collinear phase.

VI. DISCUSSION

In $CeFe_3(BO_3)_4$, the two phases of the collinear and helical phases coexist in the magnetic ordered state. From the neutron diffraction experiments we established that the domain ratio of the two phases was different in the polycrystalline and single-crystal samples. The ratio of the integrated intensities at $(0,-2,0.5)$ and $(0,-2,0.457)$ in Fig. 7(a) is 0.35 while one for the polycrystalline sample is 0.64. From this the domain ratio of the two structures for the single-crystal sample is roughly estimated to be $C_1/C_2\sim 0.3$, which is smaller than that for the polycrystalline one. This means that the ICM phase is more stable in the single-crystal sample than in the polycrystalline one. Since the polycrystalline sample was obtained by crushing the single-crystal samples, lattice strain and/or defect may affect stability of the ICM phase and the domain ratio. It is noted that the incommensurability in the isostructural $NdFe_3(BO_3)_4$ having ICM magnetic order depends on the sample size [24], and the magnetic structure of

TABLE V. The sensitivity of the refinement on the Ce^{3+} moment. $\theta_{\text{Ce-Fe}}$ is the canting angle between the Ce^{3+} and Fe^{3+} moments.

$\theta_{\text{Ce-Fe}}$	$m_{\rm Ce}$ ($\mu_{\rm B}$)	$R_{\rm mag}(\boldsymbol{k}_{\rm CM})$ (%)	$R_{\rm mag}(\boldsymbol{k}_{\rm ICM})$ (%)
0°	0.22(3)	6.29	6.81
–	0	7.78	7.41
30°	0.26(4)	6.39	6.74
60°	0.43(7)	6.56	6.67
90°	1.18(27)	8.06	7.54

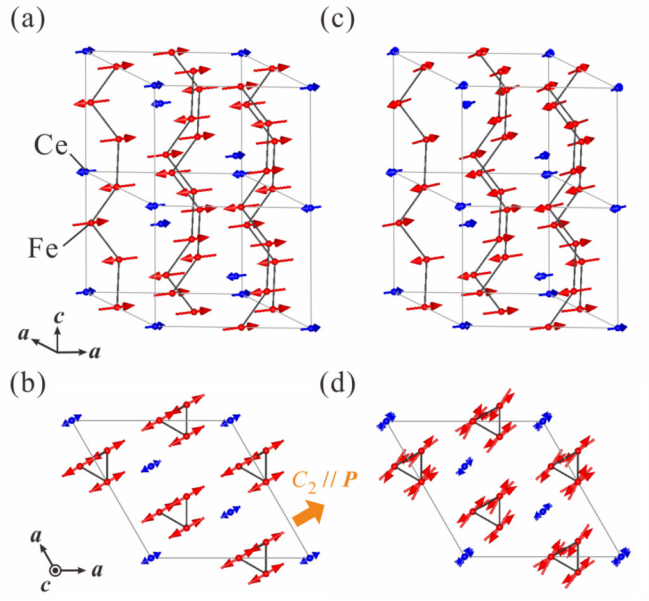

FIG. 9. The magnetic structures of $CeFe_3(^{11}BO_3)_4$. Magnetic domain having the CM propagation vector is shown in (a) and (b). The direction of the Fe^{3+} and Ce^{3+} moments in the ab plane is not determined. The case of both moments directing along the a^* axis is described here. Magnetic domain having the ICM propagation vector is shown in (c) and (d). The angle between the Fe^{3+} and Ce^{3+} moments in the ab plane is not determined. The case of the moments parallel is described here. The moment size of the Ce^{3+} ion is multiplied by ten.

$RFe_3(BO_3)_4$ may be sensitive to the shape of the sample. The reason for the difference in the domain ratio between single-crystal and polycrystalline samples is unclear, and systematic study of the sample dependence of the magnetic domain ratio would be important.

The coexistence of the CM and ICM phase has been also found in $NdFe_3(BO_3)_4$ [48]. They have suggested that the frustration of the interactions between Fe^{3+} and Nd^{3+} moments causes the phase competition between the two phases. However, the recently proposed magnetic Hamiltonian based on an inelastic neutron scattering experiment [49] does not identify the ICM structure as the ground state even though the complex network of the interactions was revealed. On the other hand, it has been suggested that the Dzyaloshinskii-Moriya (DM) interaction causes the ICM structure in Ref. [24], but no explicit evidence of the DM interaction has been found so far. Hence the origin of the ICM structure in the rare-earth ferroborates has not been identified yet. Since the incommensurability $\delta = 0.04556(16)$ at 3.7 K in $CeFe_3(BO_3)_4$ is larger than $\delta = 0.00667$ at 1.6 K in $NdFe_3(BO_3)_4$ [24], the interactions inducing the ICM structure is enhanced in $CeFe_3(BO_3)_4$ compared with $NdFe_3(BO_3)_4$. The measurement of the magnetic excitation in $CeFe_3(BO_3)_4$ by means of the inelastic neutron scattering would thus elucidate the origin of the ICM structure.

The rare-earth ferroborates other than $CeFe_3(BO_3)_4$ have exhibited multiferroic properties. Then it is reasonable to assume that $CeFe_3(BO_3)_4$ is also a multiferroic compound, and to discuss the relationship between the magnetic structure and electric polarization. Since it was suggested that the collinear antiferromagnetic structure in the ab plane leads to the spontaneous electric polarization [21], it is reasonable to assume that the polarization in $CeFe_3(BO_3)_4$ originates from the CM structure. The collinear structure in $CeFe_3(BO_3)_4$ breaks the threefold-rotational symmetry around the c axis. The magnetic subgroup that allows the symmetry reduction is nonisomorphic $C2$ when the moments align along the a or a^* axes, or $P1$ when they align along the directions other than the a and a^* axes in the ab plane. When the magnetic subgroup of the Fe and Ce sublattices in the CM structure belongs to $C2$ symmetry, the polarization appears parallel to the a or a^* axes because $C2$ symmetry allows the polarization parallel to its twofold-rotational axis. In case of $P1$ symmetry, the polarization is allowed in any directions. From the observed magnetic anisotropy in the magnetic susceptibility measurements in Fig. 3, we presume that the easy axis for the magnetic moments is along the a^* axis. In this case, the spontaneous polarization would appear along the a^* axis as shown in Fig. 9(b). The measurement of the electric polarization is necessary to confirm the orientation of the magnetic moments and demonstrate the multiferroicity of $CeFe_3(BO_3)_4$.

Control of the magnetic domain by external field such as magnetic and electric fields is of primary interest in multiferroic materials [50–54]. In $NdFe_3(BO_3)_4$, the two domains of the CM and ICM structures are controlled either by magnetic or electric fields [55]. It was found that the domain fraction of the CM phase increases, whereas that of the ICM phase decreases on applying magnetic or electric fields along the a axis. $CeFe_3(BO_3)_4$ is therefore another trial material to investigate the control of the magnetic domains with electric field.

VII. CONCLUSION

In conclusion, we have studied thermodynamic properties and magnetic structure of $CeFe_3(BO_3)_4$. The heat capacity and magnetic susceptibility measurements of the single-crystal sample indicate the antiferromagnetic transition at $T_N = 29$ K. In the neutron powder diffraction experiment, magnetic Bragg peaks with the CM and ICM propagation vectors, $\boldsymbol{k}_{CM} = (0, 0, \frac{3}{2})$ and $\boldsymbol{k}_{ICM} = (0, 0, \frac{3}{2} + \delta)$, are observed. The incommensurability evaluated to be $\delta = 0.04556(16)$ at 3.7 K decreases with increasing the temperature. Magnetic structure analysis reveals that the magnetic moments aligning in the ab plane form the collinear antiferromagnetic structure having $\boldsymbol{k}_{CM}$ and helical structure having $\boldsymbol{k}_{ICM}$. Detailed magnetic susceptibility and single-crystal neutron diffraction measurements indicate that a phase separation into the collinear and helical structures occurs. The study of the magnetic excitation is important to elucidate the origin of the ICM structure. Consideration of the multiferroicity suggests that a spontaneous polarization should appear along the a^* axis on establishing the magnetic long-range order, and the domain ratio of the collinear and helical structure would be controlled by electric field.

ACKNOWLEDGMENTS

We are grateful to D. Ueta and H. Yoshizawa for supporting the heat capacity measurement. We thank M. Hagihala

for helpful discussions in the magnetic structure analysis. We acknowledge the support of the Australian Centre for Neutron Scattering, Australian Nuclear Science and Technology Organisation, in providing the neutron research facilities used in this work. The neutron scattering experiment at the HB-3A used resources at the High Flux Isotope Reactor, a DOE office of Science User Facility operated by the ORNL (IPTS-17582.1). Travel expenses for the neutron diffraction experiments performed using ECHIDNA at ANSTO, Australia, and HB-3A at ORNL, USA were supported by the General User Program for Neutron Scattering Experiments, Institute for Solid State Physics, The University of Tokyo (Proposals No. 16911 and No. 17514), at JRR-3, Japan Atomic Energy Agency, Tokai, Japan. S.H. and S.H. were supported by the Japan Society for the Promotion of Science through the Leading Graduate Schools (MERIT).

[1] T. Kimura, T. Goto, H. Shintani, K. Ishizaka, T. Arima, and Y. Tokura, Nature (London) **426**, 55 (2003).
[2] Y. Tokura, S. Seki, and N. Nagaosa, Rep. Prog. Phys. **77**, 076501 (2014).
[3] S. Dong, J.-M. Liu, S.-W. Cheong, and Z. Ren, Adv. Phys. **64**, 519 (2015).
[4] M. Fiebig, T. Lottermoser, D. Meier, and M. Trassin, Nat. Rev. Mater. **1**, 16046 (2016).
[5] H. Katsura, N. Nagaosa, and A. V. Balatsky, Phys. Rev. Lett. **95**, 057205 (2005).
[6] M. Mostovoy, Phys. Rev. Lett. **96**, 067601 (2006).
[7] I. A. Sergienko and E. Dagotto, Phys. Rev. B **73**, 094434 (2006).
[8] C. Jia, S. Onoda, N. Nagaosa, and J. H. Han, Phys. Rev. B **76**, 144424 (2007).
[9] T. Arima, J. Phys. Soc. Jpn. **76**, 073702 (2007).
[10] R. D. Johnson and P. G. Radaelli, Annu. Rev. Mater. Res. **44**, 269 (2014).
[11] A. K. Zvezdin, S. S. Krotov, A. M. Kadomtseva, G. P. Vorob'ev, Yu. F. Popov, A. P. Pyatakov, L. N. Bezmaternykh, and E. A. Popova, JETP Lett. **81**, 272 (2005).
[12] A. K. Zvezdin, G. P. Vorob'ev, A. M. Kadomtseva, Yu. F. Popov, A. P. Pyatakov, L. N. Bezmaternykh, A. V. Kuvardin, and E. A. Popova, JETP Lett. **83**, 509 (2006).
[13] A. M. Kadomtseva, A. K. Zvezdin, A. P. Pyatakov, A. V. Kuvardin, G. P. Vorob'ev, Yu. F. Popov, and L. N. Bezmaternykh, JETP **105**, 116 (2007).
[14] A. K. Zvezdin, A. M. Kadomtseva, Yu. F. Popov, G. P. Vorob'ev, A. P. Pyatakov, V. Yu. Ivanov, A. M. Kuz'menko, A. A. Mukhin, L. N. Bezmaternykh, and I. A. Gudim, JETP **109**, 68 (2009).
[15] A. M. Kadomtseva, Yu. F. Popov, G. P. Vorob'ev, A. P. Pyatakov, S. S. Krotov, and K. I. Kamilov, Low Temp. Phys. **36**, 511 (2010).
[16] U. Adem, L. Wang, D. Fausti, W. Schottenhamel, P. H. M. van Loosdrecht, A. Vasiliev, L. N. Bezmaternykh, B. Büchner, C. Hess, and R. Klingeler, Phys. Rev. B **82**, 064406 (2010).
[17] Yu. F. Popov, A. P. Pyatakov, A. M. Kadomtseva, G. P. Vorob'ev, A. K. Zvezdin, A. A. Mukhin, V. Yu. Ivanov, and I. A. Gudim, JETP **111**, 199 (2010).
[18] A. A. Mukhin, G. P. Vorob'ev, V. Yu. Ivanov, A. M. Kadomtseva, A. S. Narizhnaya, A. M. Kuz'menko, Yu. F. Popov, L. N. Bezmaternykh, and I. A. Gudim, JETP Lett. **93**, 275 (2011).
[19] V. Yu. Ivanov, A. M. Kuzmenko, and A. A. Mukhin, JETP Lett. **105**, 435 (2017).
[20] A. I. Popov, D. I. Plokhov, and A. K. Zvezdin, Phys. Rev. B **87**, 024413 (2013).
[21] T. Kurumaji, K. Ohgushi, and Y. Tokura, Phys. Rev. B **89**, 195126 (2014).
[22] C. Ritter, A. Vorotynov, A. Pankrats, G. Petrakovskiĭ, V. Temerov, I. Gudim, and R. Szymczak, J. Phys.: Condens. Matter **22**, 206002 (2010).
[23] P. Fischer, V. Pomjakushin, D. Sheptyakov, L. Keller, M. Janoschek, B. Roessli, J. Schefer, G. Petrakovskii, L. Bezmaternikh, V. Temerov, and D. Velikonov, J. Phys.: Condens. Matter **18**, 7975 (2006).
[24] M. Janoschek, P. Fischer, J. Schefer, B. Roessli, V. Pomjakushin, M. Meven, V. Petricek, G. Petrakovskii, and L. Bezmaternikh, Phys. Rev. B **81**, 094429 (2010).
[25] C. Ritter, A. Pankrats, I. Gudim, and A. Vorotynov, J. Phys.: Condens. Matter **24**, 386002 (2012).
[26] M. N. Popova, B. Z. Malkin, K. N. Boldyrev, T. N. Stanislavchuk, D. A. Erofeev, V. L. Temerov, and I. A. Gudim, Phys. Rev. B **94**, 184418 (2016).
[27] H. Mo, C. S. Nelson, L. N. Bezmaternykh, and V. T. Temerov, Phys. Rev. B **78**, 214407 (2008).
[28] C. Ritter, A. Balaev, A. Vorotynov, G. Petrakovskiĭ, D. Velikanov, V. Temerov, and I. Gudim, J. Phys.: Condens. Matter **19**, 196227 (2007).
[29] C. Ritter, A. Pankrats, I. Gudim, and A. Vorotynov, J. Phys.: Conf. Ser. **340**, 012065 (2012).
[30] C. Ritter, A. Vorotynov, A. Pankrats, G. Petrakovskiĭ, V. Temerov, I. Gudim, and R. Szymczak, J. Phys.: Condens. Matter **20**, 365209 (2008).
[31] T. Usui, Y. Tanaka, H. Nakajima, M. Taguchi, A. Chainani, M. Oura, S. Shin, N. Katayama, H. Sawa, Y. Wakabayashi, and T. Kimura, Nat. Mater. **13**, 611 (2014).
[32] K. N. Boldyrev, T. N. Stanislavchuk, A. A. Sirenko, D. Kamenskyi, L. N. Bezmaternykh, and M. N. Popova, Phys. Rev. Lett. **118**, 167203 (2017).
[33] A. M. Kuzmenko, D. Szaller, Th. Kain, V. Dziom, L. Weymann, A. Shuvaev, A. Pimenov, A. A. Mukhin, V. Yu. Ivanov, I. A. Gudim, L. N. Bezmaternykh, and A. Pimenov, Phys. Rev. Lett. **120**, 027203 (2018).
[34] J. A. Campá, C. Cascales, E. Gutiérrez-Puebla, M. A. Monge, I. Rasines, and C. Ruíz-Valero, Chem. Mater. **9**, 237 (1997).
[35] Y. Hinatsu, Y. Doi, K. Ito, K. Wakeshima, and A. Alemi, J. Solid State Chem. **172**, 438 (2003).
[36] L. N. Bezmaternykh, S. A. Kharlamova, and V. L. Temerov, Crystallogr. Rep. **49**, 855 (2004).
[37] J. Rodriguez-Carvajal, Physica B (Amsterdam) **192**, 55 (1993).
[38] A. Wills, Physica B (Amsterdam) **276-278**, 680 (2000).
[39] B. C. Chakoumakos, H. Cao, F. Ye, A. D. Stoica, M. Popovici, M. Sundaram, W. Zhou, J. S. Hicks, G. W.

Lynn, and R. A. Riedel, J. Appl. Crystallogr. **44**, 655 (2011).

[40] R. Z. Levitin, E. A. Popova, R. M. Chtsherbov, A. N. Vasiliev, M. N. Popova, E. P. Chukalina, S. A. Klimin, P. H. M. van Loosdrecht, D. Fausti, and L. N. Bezmaternykh, JETP Lett. **79**, 423 (2004).

[41] E. A. Popova, D. V. Volkov, A. N. Vasiliev, A. A. Demidov, N. P. Kolmakova, I. A. Gudim, L. N. Bezmaternykh, N. Tristan, Yu. Skourski, B. Buchner, C. Hess, and R. Klingeler, Phys. Rev. B **75**, 224413 (2007).

[42] E. A. Popova, N. Tristan, A. N. Vasiliev, V. L. Temerov, L. N. Bezmaternykh, N. Leps, B. Buchner, and R. Klingeler, Eur. Phys. J. B **62**, 123 (2008).

[43] A. N. Vasiliev, E. A. Popova, L. N. Bezmaternykh, V. L. Temerov, and Z. Hiroi, JETP **102**, 262 (2006).

[44] N. Tristan, R. Klingeler, C. Hess, B. Büchner, E. Popova, I. A. Gudim, and L. N. Bezmaternykh, J. Magn. Magn. Mater. **316**, e621 (2007).

[45] D. V. Volkov, E. A. Popova, N. P. Kolmakova, A. A. Demidov, T. Tristan, Yu. Skourski, B. Buechner, I. A. Gudim, and L. N. Bezmaternykh, J. Magn. Magn. Mater. **316**, e717 (2007).

[46] A. Pankrats, G. Petrakovskii, A. Kartashev, E. Eremin, and V. Temerov, J. Phys.: Condens. Matter **21**, 436001 (2009).

[47] E. A. Popova, A. N. Vasiliev, V. L. Temerov, L. N. Bezmaternykh, N. Tristan, R. Klingeler, and B. Büchner, J. Phys.: Condens. Matter **22**, 116006 (2010).

[48] J. E. Hamann-Borrero, S. Partzsch, S. Valencia, C. Mazzoli, J. Herrero-Martin, R. Feyerherm, E. Dudzik, C. Hess, A. Vasiliev, L. Bezmaternykh, B. Büchner, and J. Geck, Phys. Rev. Lett. **109**, 267202 (2012).

[49] I. V. Golosovsky, A. K. Ovsyanikov, D. N. Aristov, P. G. Matveeva, A. A. Mukhin, M. Boehm, L.-P. Regnault, and L. N. Bezmaternykh, J. Magn. Magn. Mater. **451**, 443 (2018).

[50] Y. H. Chu, L. W. Martin, M. B. Holcomb, M. Gajek, S. J. Han, Q. He, N. Balke, C. H. Yang, D. Lee, W. Hu, Q. Zhan, P. L. Yang, A. Fraile-Rodriguez, A. Scholl, S. X. Wang, and R. Ramesh, Nat. Mater. **7**, 478 (2008).

[51] P. G. Radaelli, L. C. Chapon, A. Daoud-Aladine, C. Vecchini, P. J. Brown, T. Chatterji, S. Park, and S.-W. Cheong, Phys. Rev. Lett. **101**, 067205 (2008).

[52] F. Fabrizi, H. C. Walker, L. Paolasini, F. de Bergevin, A. T. Boothroyd, D. Prabhakaran, and D. F. McMorrow, Phys. Rev. Lett. **102**, 237205 (2009).

[53] Y. Tokunaga, Y. Taguchi, T.-H. Arima, and Y. Tokura, Nat. Phys. **8**, 838 (2012).

[54] Y. S. Chai, S. Kwon, S. H. Chun, I. Kim, B.-G. Jeon, K. H. Kim, and S. Lee, Nat. Commun. **5**, 4208 (2014).

[55] S. Partzsch, J.-E. Hamann-Borrero, C. Mazzoli, J. Herrero-Martin, S. Valencia, R. Feyerherm, E. Dudzik, A. Vasiliev, L. Bezmaternykh, B. Buchner, and J. Geck, Phys. Rev. B **94**, 054421 (2016).